SCIENCE CHINA
Physics, Mechanics & Astronomy

•Article•

July 2023 Vol. 66 No. 7: 274212
https://doi.org/10.1007/s11433-023-2093-9

Unidirectional transport in amorphous topological photonic crystals

Yuting Yang[1*], Xinyue Qian[1], Liwei Shi[1], Xiaopeng Shen[1], and Zhi Hong Hang[2,3*]

[1]*School of Materials Science and Physics, China University of Mining and Technology, Xuzhou 221116, China;*
[2]*School of Physical Science and Technology & Collaborative Innovation Center of Suzhou Nano Science and Technology, Soochow University, Suzhou 215006, China;*
[3]*Institute for Advanced Study, Soochow University, Suzhou 215006, China*

Received January 4, 2023; accepted March 3, 2023; published online May 26, 2023

Many works on topological insulators have focused on periodic lattice systems, where short- and long-range order is considered. Here we construct a two-dimensional amorphous photonic crystal with short-range order and a controllable level of long-range order and experimentally investigate the transport of topological edge states in this amorphous system. We demonstrate that topology properties remain constant with unidirectional edge state propagation, immune to specific disorder strength. The partition phenomena of edge states are also observed at the intersection of four topological channels in microwave experiments. This proposed amorphous configuration provides new opportunities to explore the relationship between short-range order and topology and may alleviate the fabrication difficulties of topological optical devices for practical applications.

photonic crystal, amorphous material, topological insulator

PACS number(s): 42.70.Qs, 61.43.Dq, 03.65.Vf

Citation: Y. Yang, X. Qian, L. Shi, X. Shen, and Z. H. Hang, Unidirectional transport in amorphous topological photonic crystals, Sci. China-Phys. Mech. Astron. **66**, 274212 (2023), https://doi.org/10.1007/s11433-023-2093-9

1 Introduction

The topological insulator, whose striking feature is that the edge state is topologically protected and immune to defects and perturbations, has attracted intense research interest [1-3]. A topological photonic crystal (PhC) is a periodic structure with long-range order related to the lattice periodicity and short-range order connected to neighboring sites within a unit cell [4-23]. It provides a good platform for realizing many devices in practical applications, such as topological lasers [24,25]. Topological photonics have also been extended into aperiodic photonic structures, including the photonic quasicrystals possessing hidden long-range order but no translational symmetry [26-29] and the topological Anderson insulator with completely random sites [30-32].

The short-range disorder is usually introduced into topological PhC lattices to verify the robustness of topological edge states to perturbations. The question is, what spatial order is required to induce topological edge states? The amorphous PhCs only possess short-range order, but no long-range order has been proposed to study this interesting question [33]. The short-range order in an amorphous PhC, for example, can be used to improve light confinement and realize a laser [34,35]. Amorphous gyromagnetic photonic lattices have been created to study the nonreciprocal robustness of edge states theoretically [36-38] and experi-

---

*Corresponding authors (Zhi Hong Hang, email: zhhang@suda.edu.cn; Yuting Yang, email: yangyt@cumt.edu.cn) mentally [39]. Because of the applied magnetic field, the time-reversal symmetry of the amorphous gyromagnetic photonic crystal is broken, and the lack of pure dielectric material in the system limits applications in optical devices. Additionally, the amorphous topological valley PhC was used to study the effect of long-range deformations. However, because of the mismatch between the lattice and the chiral exciting source, the unidirectional transport of edge states was not observed experimentally [40].

Here, we determine that topological photonic bandgaps in a two-dimensional (2D) amorphous PhC continue to exist if sufficient short-range order exists and only specific disorder strength is applied. Our designed amorphous PhC comprises a pure dielectric material, and the time-reversal symmetry is not broken. An amorphous lattice is constructed by molecular dynamics simulations to adjust short-range order to study the variation in the bandgap [37,39]. In our study, we use a more convenient method by rotating lattices to realize an amorphous PhC, in which short-range order remains unchanged at the designed parameter. Thus, we can manipulate the disorder strength to study the nature of the topological bandgap. Microwave experiments are implemented to verify the unidirectional transport of the topological edge states at a low degree of disorder, which to our knowledge, is the first experimental realization of topological amorphous PhC with a dielectric material. Additionally, the partition of edge states is directly observed in amorphous PhCs comprising four domains. This phenomenon may help us find more interesting applications for designing optical devices in the future.

2 Design of an amorphous PhC

We choose a hexagonal unit cell as the original structure without disorder arranged in a triangular lattice of a 2D periodic PhC, whose lattice constant is a, as shown in the left panel of Figure 1(a). A unit cell is composed of six cylinders made of dielectric material with relative permittivity $\varepsilon = 7.5$ and diameter $d = 0.24a$, embedded in an air background. When the distance h_1 between neighboring cylinders within a unit cell is larger than the distance h_2 between nearest cylinders in the neighboring unit cell, the periodic PhC is topological and otherwise trivial. The distance h_1 (h_2) is taken as $0.36a$ ($0.28a$) in a topological PhC and $0.30a$ ($0.40a$) in a trivial PhC. The band diagram of the topological PhC with a transverse magnetic mode (E_z is the electric field along the z direction) is calculated using COMSOL Multiphysics, as displayed in Figure 1(b), and has a topological bandgap indicated in green. Topological edge states emerge in the interface formed by topological and trivial PhCs. Figure 1(c) shows the dispersion diagram of the edge states calculated by the supercell method. The same structures have been applied to construct a topological PhC to experimentally realize a unidirectional electromagnetic waveguide [16].

PhCs are unique because of their photonic bandgap, whose size is determined by the lattice structure and refractive index contrast of the dielectric material [41]. Long-range order related to lattice periodicity is unnecessary for bandgap formation, and thus amorphous semiconductor structures still possess electronic bandgaps [42]. Because of the choice

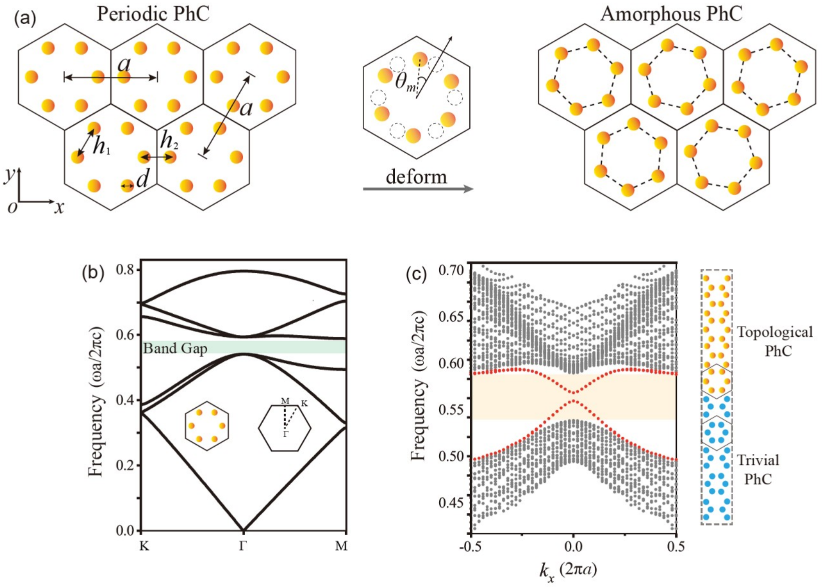

Figure 1 (Color online) (a) Left panel: Schematic of a periodic PhC with the triangular lattice. A hexagonal unit cell with lattice constant a comprises six dielectric cylinders with diameter d=0.24a and relative permittivity ε=7.5. The distance h_1 (h_2) is taken as 0.36a (0.28a) to form a topological PhC, while 0.30a (0.40a) is taken to form a trivial PhC. Right panel: Schematic of an amorphous PhC created by rotating six cylinders around the center of a unit cell. The maximum rotation angle of the six cylinders is defined as θ_m. (b) Transverse magnetic band diagram of a periodic topological PhC exhibiting a photonic bandgap highlighted in green. Inset: Unit cell and the first Brillouin zone. (c) Dispersion of edge states calculated by a supercell composed of topological and trivial PhCs, denoted by yellow and blue cylinders in the right panel, respectively.

of high refractive index contrast, the size of the bandgap is very large in our design of topological PhCs. When we construct a PhC with sufficient short-range order linked with neighboring cylinders, the bandgap continues to exist due to the evanescent coupling of the Mie resonances of individual dielectric cylinders [34,35]. This structure is considered a new material called photonic glass [43].

Our proposed amorphous PhC is constructed by randomly rotating six cylinders against the center of the hexagonal unit cell, as displayed in the right panel of Figure 1(a). The random rotation angle is defined as $\theta = R\theta_m$, where θ_m is the controlling angle, and R is a random number uniformly distributed between −1 and 1. Thus, the rotation angles of dielectric cylinders in the entire lattice are randomly distributed between $-\theta_m$ and θ_m. It is easily recognized that the disorder strength in different amorphous PCs can be parameterized by the maximum rotation angle θ_m. Although amorphous PhCs differ in detailed structures, they possess the same short-range order generated by a fixed distance h_1 between neighboring cylinders within a unit cell. In other words, in our scheme to construct an amorphous PhC, the short-range order is fixed, while the level of the long-range order decreases with increasing θ_m.

3 Edge state transport in amorphous PhCs

With local rotation in unit cells, the photonic bandgaps of an amorphous PhC structure cannot be directly calculated. Thus, a source to excite electric fields is placed at the center of the amorphous PhC, and the total energy flow is detected along the circular integral path illustrated by the inset of Figure 2(a). Figure 2(a) shows the radiation power spectrum of amorphous PhCs at different maximum rotation angles θ_m of six cylinders in a unit cell, in which energy flow is averaged over ten independent configurations. A prominent dip in the spectrum highlighted in green at θ_m =10° represents a full bandgap. The disordered degree of the amorphous PhC

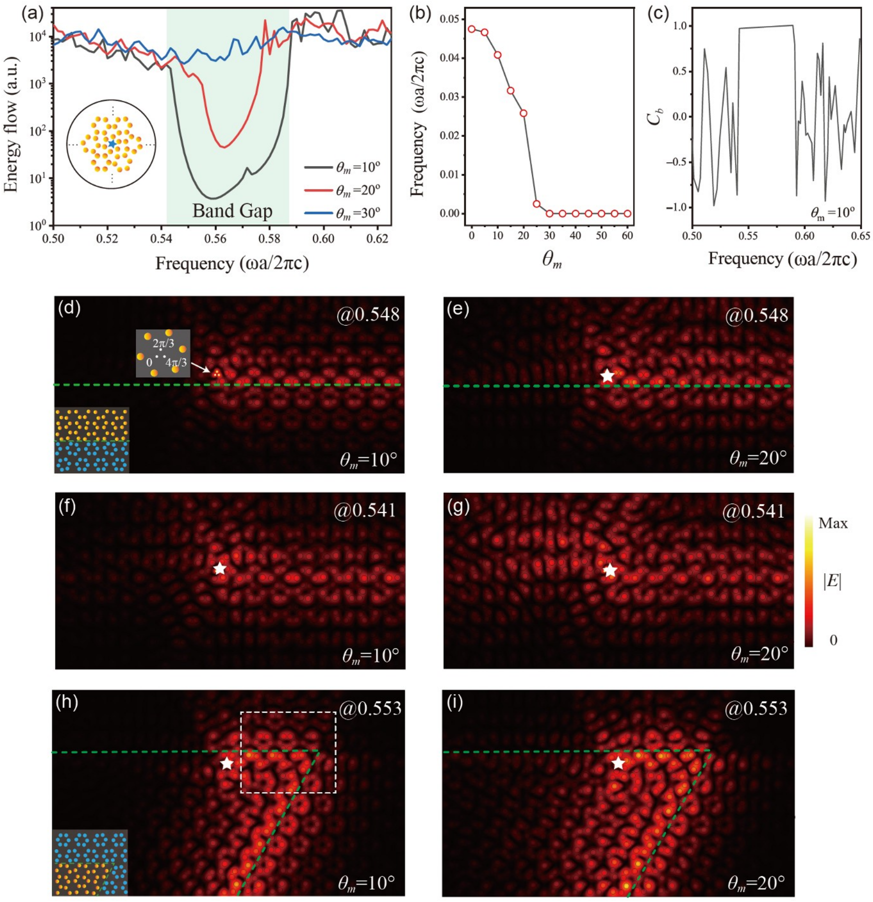

Figure 2 (Color online) (a) Energy flow spectrum at maximum rotation angles of dielectric cylinders in amorphous topological PhCs at θ_m=10°, 20°, and 30°. The green region represents the topological bandgap of an amorphous PhC at θ_m=10°. Inset: Schematic of an amorphous configuration. The location of the exciting source is marked by a green star. The integral of the energy flow is along the circular path. With the increasing disordered degree, the photonic bandgap rapidly shrinks and finally disappears. (b) Photonic bandgap as a function of maximum rotation angles. (c) Bott index of an amorphous PhC. (d)-(g) Simulated electric fields E_z for transporting the edge state of amorphous PhCs at θ_m=10° and 20° and different frequencies. Inset: Schematic of the amorphous structure with distinct topological domains. The location of the chiral source is denoted by a white star. (h), (i) The edge states remain unchanged when traveling around sharp turns in amorphous PhCs at θ_m=10° and 20°.

increases by controlling the rotation of dielectric cylinders to obtain a larger θ_m, and thus the width of the photonic bandgap shrinks to a narrow range and nearly disappears at θ_m=30°, confirming that photonic gaps are induced by short-range order. Figure 2(b) also illustrates that the photonic bandgap is a function of the maximum rotation angles of dielectric cylinders in amorphous topological PhCs. To characterize the topological properties of amorphous PhCs, we use the Bott index [44-46] (C_b), which is identical to the Chern number but defined in real space. When the C_b at a specific θ_m and frequency is calculated, all eigenelectric fields below this eigenfrequency should be computed. Two unitary matrices are defined as $U_X = \mathrm{e}^{2\pi \mathrm{i}x/L_x}$ and $U_Y = \mathrm{e}^{2\pi \mathrm{i}y/L_y}$, where x and y are the spatial coordinates of $L_x \times L_y$ lattice sites. P is the projection operator of all eigenstates below a specific frequency. The eigenstates of the electric fields of an amorphous PhC can be directly obtained from numerical simulations and need averaging over many configurations. Then, block matrices are given by $\widetilde{U}_X = PU_XP$ and $\widetilde{U}_Y = PU_YP$. Finally, the Bott index is computed as $C_b = \mathrm{ImTrln}(\widetilde{U}_Y\widetilde{U}_X\widetilde{U}^{\dagger}{}_Y\widetilde{U}^{\dagger}{}_X) / (2\pi)$. Figure 2(c) shows the Bott index for an amorphous PhC with θ_m=10°, in which the bandgap is topological (C_b=1).

The photonic bandgap shrinks as random rotations are introduced. However, the corresponding topological properties existing in a periodic PhC structure remain in amorphous PhCs as long as the photonic bandgap exists. Assembling two amorphous PhCs with distinct topology at a low degree of disorder, topological edge states persist along the interface. The simulated spatial distribution of electric field E_z is shown in Figure 2(d) at a normalized frequency of 0.548 for θ_m=10°. A chiral source indicated by a white star is applied to selectively excite topological edge states with a specific pseudospin. The excited edge state unidirectionally propagates along the interface. When the maximum rotation angle of dielectric cylinders increases to θ_m=20°, the edge state remains unidirectional, but its mode profile does not decay into bulk PhC structures as rapidly as the θ_m=10° case, reflecting a relatively small photonic bandgap, as displayed in Figure 2(e) at a normalized frequency of 0.548. Additionally, with increasing disordered strength, the frequency range of edge states and the photonic bandgap size simultaneously become narrower. Figure 2(f) and (g) show the compared electric field at the same frequency of 0.541 but different rotation angles θ_m=10° and 20°, where bulk modes are excited simultaneously because of the smaller photonic gap. To demonstrate the robustness of topological edge states in an amorphous PhC, a configuration with a sharp bend is considered. In Figure 2(h) and (i) at θ_m=10° and 20°, respectively, we observe that the edge states remain unidirectional and travel around a sharp turn nearly without scattering at a normalized frequency of 0.553. This result reveals that edge states in an amorphous PhC remain topologically protected and immune to backscattering.

Microwave experiments are performed to demonstrate the transport properties of topological edge states in an amorphous PhC. The experimental setup and sample are displayed in Figure 3(a) and (b), respectively. The PhC sample is made of alumina cylinders with a relative permittivity ε=7.5, diameter d=6 mm, and height h=8 mm. The lattice constant of the amorphous PhC is a=25 mm. The distance h_1 (h_2) is taken as 9 mm (7 mm) in a topological PhC and 7.5 mm (10 mm) in a trivial PhC. The PhC structure is surrounded by perfectly matched layers to absorb scattering waves and sandwiched between two parallel metallic plates, which form a waveguide. Topological and trivial amorphous PhCs are highlighted in yellow and blue regions, respectively, and a green dashed line represents their interface. A chiral source indicated by a white star is produced by three antennas with different phase delays and employed to selectively excite topological edge states with a specific pseudospin. The antenna array and its measured electric field distribution are displayed in the left panels in Figure 3(b). Figure 3(c) shows the measured distribution of the intensity of electric field E_z at 8.01 GHz and the maximum rotation angle θ_m=10° of alumina cylinders in an amorphous configuration. The topological edge state only propagates in the forward direction and is suppressed backward. Because of a small air gap between the top metal plate and sample, the frequency of edge states undergoes redshifts, but their properties remain constant. The phenomena of edge states in experimental measurements agree well with simulations. When the maximum rotation angle is set as θ_m=20°, our experimental results verify that the edge states still mainly propagate along the interface, as shown in Figure 3(d). Consistent with the simulations, the frequency range of edge states in experiments becomes narrower with a higher degree of disorder. Figure 2(e) and (f) show the measured electric field along the y direction marked by white dashed lines in Figure 2(c) and (d). The strength of the electric field quickly decays into amorphous PhCs, manifesting the good confinement of the edge state at the interface.

4 Partition of edge states in amorphous PhCs

The transmission partition of edge states dependent on the geometry at topological channel intersections has been studied in graphene [47] and acoustic crystals [48]. Here, we demonstrate that such unidirectional topological transport of the edge state can be realized in an amorphous PhC. Figure 4(a) illustrates the detailed structure, in which four channels intersect obliquely and separate topological and trivial amorphous PhCs into four domains denoted by yellow and

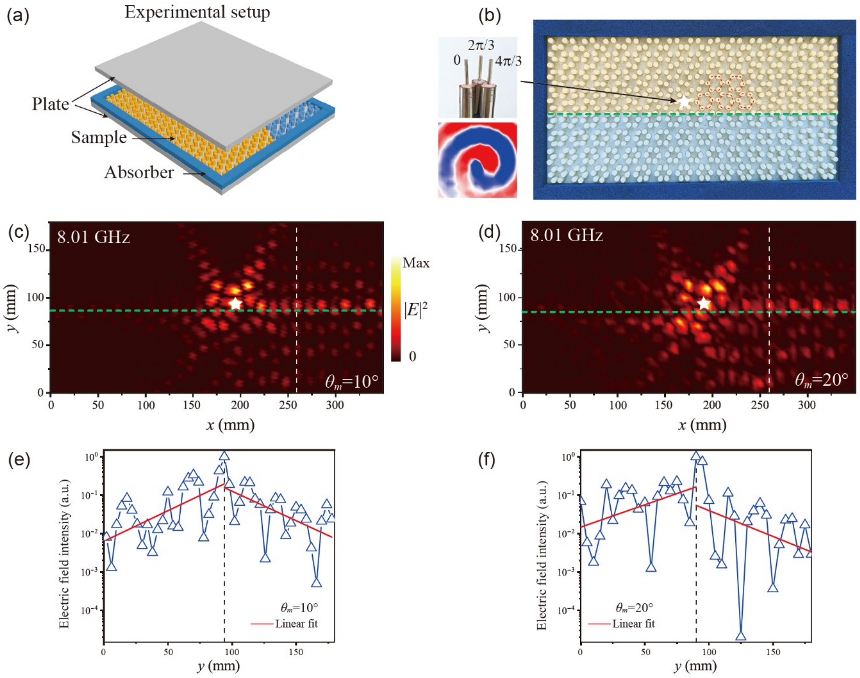

Figure 3 (Color online) (a) Schematic of the experimental setup. The experimental sample is placed in two metallic plates and surrounded by an absorber. (b) Photograph of the alumina cylinders of the amorphous PhC. Left panel: An antenna array and a measured electric field of the chiral source. (c), (d) Experimental measurements of E_z field intensity distributions of edge states in amorphous PhCs with maximum rotation angles of θ_m=10° and 20°. The electric field intensity in the forward direction is much stronger than that in the backward direction. This result experimentally demonstrates that the edge state unidirectionally propagates along the interface of topological and trivial amorphous PhCs. (e), (f) Intensity of the electric field in the y direction.

blue circles, respectively. The excited edge state travels from the leftward channel labeled L to upward (U) and downward (D) channels but is nearly suppressed on the right channels (R). A similar phenomenon has been achieved in topological valley photonic systems to manipulate photonic valley pseudospins [12,49,50]. With the intersection angles of the four channels at $\alpha=\beta=60°$, the simulated distribution of the electric field magnitude of edge states at a normalized frequency of 0.547 and θ_m=10° is displayed in Figure 4(b). The transmitted energy proportion of individual channels is calculated, and the transmission proportion of channel D is approximately 0.6, which is larger than that in channel U by approximately 0.3. As the disorder strength increases, the edge state along channel L is much easier to couple into channel D, and gradually, the partition is destroyed, as shown in Figure 4(c) at θ_m=30°. When the intersection angles are α=120° and β=60°, the transmission proportion of channels U and D is inverted with α=60°. Figure 4(d) characterizes that the E_z field magnitude of the edge state on channel U in this structure is much stronger at θ_m=10°. At $\alpha=\beta=90°$, the edge state bisects equally into the U and D channels, as displayed in Figure 4(e). Because of the broken symmetry of the lattice on the vertical intersection interface, the edge states on the four channels are weak and comparable in intensity to the exciting source. The partition phenomenon of edge states depends on the geometry of amorphous structures and can be adjusted by the intersection angles of the four channels in different amorphous configurations. These transport phenomena can be used to design optical devices in applications to manipulate electromagnetic waves, such as

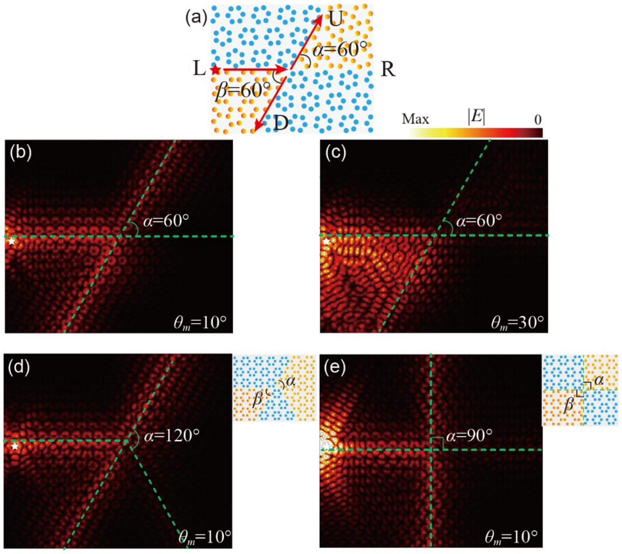

Figure 4 (Color online) (a) Schematic of the partition configuration of edge states. Four domains are composed of amorphous PhCs with distinct topology and the same maximum rotation angles of dielectric cylinders in a unit cell. Four channels are labeled by L (left), R (right), U (up), and D (down). (b), (c) Simulated distributions of the electric field magnitude at $\alpha=\beta=60°$, but θ_m=10° and 30°, respectively. (d) Electric field distribution at α=120°, β=60°, and θ_m=10°. (e) Electric field distribution at $\alpha=\beta=90°$ and θ_m=10°. All simulated frequencies are 0.547.

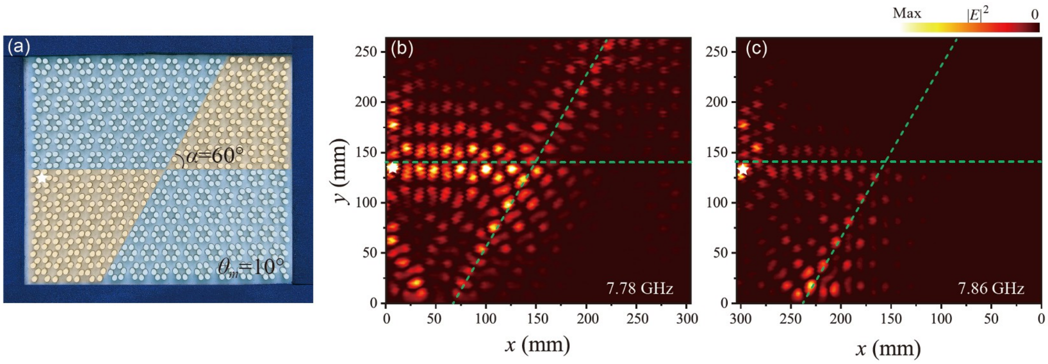

Figure 5 (Color online) (a) Photograph of the experimental sample to partition edge states in amorphous PhCs. Four channels divide the structure into four domains possessing distinct topological properties marked by yellow and blue regions. The location of the exciting source is indicated by a white star. (b), (c) Measured electric field intensity E_z of the edge state partition in experiments at 7.78 and 7.86 GHz.

beam splitters and interferometers.

We implement experiments to directly observe the partition phenomenon of edge states at the intersections of topological channels in amorphous PhCs. Figure 5(a) shows the amorphous PhC lattices comprising alumina cylinders whose parameters are identical to those in Figure 3. Four channels are built by amorphous topological PhCs and trivial PhCs denoted by yellow and blue regions, respectively. We consider that the intersection angles of the four channels are $\alpha=\beta=60°$. The maximum rotation angle of this amorphous configuration is set as $\theta_m=10°$. Figure 5(b) shows the distribution of the intensity of electric field E_z in experimental measurements at a frequency of 7.78 GHz. At this low disordered degree, we observe that the edge state excited by an antenna source propagates in the upward and downward directions, which agrees well with simulations. Beyond this frequency range of the partition behavior, the edge state is easier to couple to the downward channel at lower and higher frequencies, for example, 7.86 GHz, as shown in Figure 5(c).

5 Conclusions

In this study, we experimentally realized an amorphous PC whose long-range order interactions can be tuned. A sophisticated but simple creation method, which randomly rotates all-dielectric cylinders in a unit cell, is designed that guarantees the short-range order is preserved, but the long-range order can be controlled by rotation angles. By controlling the rotation angles, the disorder strength can be increased where the photonic gap becomes narrower and is closed finally, leading to the shrinkage and disappearance of edge state dispersion. We directly observed the unidirectional propagation and the partition of topological edge states in the amorphous configuration, in which similar backscattering-immune properties are visualized. This new scheme provides a platform for studying additional properties of amorphous topological PhCs. There is no need to include perfect periodicity. Our discovery may help alleviate the fabrication difficulties of practical topological optical devices.

This work was supported by the Key Academic Discipline Project of China University of Mining and Technology (Grant No. 2022WLXK06), the National Natural Science Foundation of China (Grant Nos. 11874274, 12004425, and 12274315), the Natural Science Foundation of Jiangsu Province (Grant No. BK20200630), the Qing Lan Project, a Project Funded by the Priority Academic Program Development of Jiangsu Higher Education Institutions (PAPD), and the Basic Research Program of Xuzhou (Grant No. KC22016). We would like to thank Prof. Peiheng Zhou and Dr. Gui-Geng Liu for their help.

1 M. Z. Hasan, and C. L. Kane, Rev. Mod. Phys. **82**, 3045 (2010).
2 X. L. Qi, and S. C. Zhang, Rev. Mod. Phys. **83**, 1057 (2011).
3 S. Raghu, and F. D. M. Haldane, Phys. Rev. A **78**, 033834 (2008).
4 Z. Wang, Y. Chong, J. D. Joannopoulos, and M. Soljačić, Nature **461**, 772 (2009).
5 Y. Poo, R. Wu, Z. Lin, Y. Yang, and C. T. Chan, Phys. Rev. Lett. **106**, 093903 (2011).
6 C. L. Kane, and E. J. Mele, Phys. Rev. Lett. **95**, 226801 (2005).
7 B. A. Bernevig, T. L. Hughes, and S. C. Zhang, Science **314**, 1757 (2006).
8 A. B. Khanikaev, S. Hossein Mousavi, W. K. Tse, M. Kargarian, A. H. MacDonald, and G. Shvets, Nat. Mater. **12**, 233 (2013).
9 W. J. Chen, S. J. Jiang, X. D. Chen, B. Zhu, L. Zhou, J. W. Dong, and C. T. Chan, Nat. Commun. **5**, 5782 (2014).
10 L. Lu, J. D. Joannopoulos, and M. Soljačić, Nat. Photon. **8**, 821 (2014).
11 L. H. Wu, and X. Hu, Phys. Rev. Lett. **114**, 223901 (2015).
12 X. Cheng, C. Jouvaud, X. Ni, S. H. Mousavi, A. Z. Genack, and A. B. Khanikaev, Nat. Mater. **15**, 542 (2016).
13 S. Yves, R. Fleury, T. Berthelot, M. Fink, F. Lemoult, and G. Lerosey, Nat. Commun. **8**, 16023 (2017).
14 A. B. Khanikaev, and G. Shvets, Nat. Photon. **11**, 763 (2017).
15 F. Gao, H. Xue, Z. Yang, K. Lai, Y. Yu, X. Lin, Y. Chong, G. Shvets, and B. Zhang, Nat. Phys. **14**, 140 (2018).
16 Y. Yang, Y. F. Xu, T. Xu, H. X. Wang, J. H. Jiang, X. Hu, and Z. . Hang, Phys. Rev. Lett. **120**, 217401 (2018).
17 S. Peng, N. J. Schilder, X. Ni, J. van de Groep, M. L. Brongersma, A. Alù, A. B. Khanikaev, H. A. Atwater, and A. Polman, Phys. Rev. Lett. **122**, 117401 (2019).
18 M. I. Shalaev, W. Walasik, A. Tsukernik, Y. Xu, and N. M. Litch-

initser, Nat. Nanotech. **14**, 31 (2019).
19 X. T. He, E. T. Liang, J. J. Yuan, H. Y. Qiu, X. D. Chen, F. L. Zhao, and J. W. Dong, Nat. Commun. **10**, 872 (2019).
20 Y. Yang, Z. Jia, Y. Wu, R. C. Xiao, Z. H. Hang, H. Jiang, and X. C. Xie, Sci. Bull. **65**, 531 (2020).
21 B. Xie, G. Su, H. F. Wang, F. Liu, L. Hu, S. Y. Yu, P. Zhan, M. H. Lu, Z. Wang, and Y. F. Chen, Nat. Commun. **11**, 3768 (2020).
22 Y. T. Yang, D. J. Zhu, Z. H. Hang, and Y. D. Chong, Sci. China-Phys. Mech. Astron. **64**, 257011 (2021).
23 X. T. He, J. W. Liu, F. L. Shi, K. Shen, W. J. Chen, X. D. Chen, and J. W. Dong, Sci. China-Phys. Mech. Astron. **65**, 284212 (2022).
24 Y. Zeng, U. Chattopadhyay, B. Zhu, B. Qiang, J. Li, Y. Jin, L. Li, A. G. Davies, E. H. Linfield, B. Zhang, Y. Chong, and Q. J. Wang, Nature **578**, 246 (2020).
25 Z. K. Shao, H. Z. Chen, S. Wang, X. R. Mao, Z. Q. Yang, S. L. Wang, X. X. Wang, X. Hu, and R. M. Ma, Nat. Nanotechnol. **15**, 67 (2020).
26 Y. S. Chan, C. T. Chan, and Z. Y. Liu, Phys. Rev. Lett. **80**, 956 (1998).
27 M. E. Zoorob, M. D. B. Charlton, G. J. Parker, J. J. Baumberg, and M. C. Netti, Nature **404**, 740 (2000).
28 M. Notomi, H. Suzuki, T. Tamamura, and K. Edagawa, Phys. Rev. Lett. **92**, 123906 (2004).
29 J. W. Dong, M. L. Chang, X. Q. Huang, Z. H. Hang, Z. C. Zhong, W. J. Chen, Z. Y. Huang, and C. T. Chan, Phys. Rev. Lett. **114**, 163901 (2015).
30 J. Li, R. L. Chu, J. K. Jain, and S. Q. Shen, Phys. Rev. Lett. **102**, 136806 (2009).
31 S. Stützer, Y. Plotnik, Y. Lumer, P. Titum, N. H. Lindner, M. Segev, M. C. Rechtsman, and A. Szameit, Nature **560**, 461 (2018).
32 G. G. Liu, Y. Yang, X. Ren, H. Xue, X. Lin, Y. H. Hu, H. Sun, B. Peng, P. Zhou, Y. Chong, and B. Zhang, Phys. Rev. Lett. **125**, 133603 (2020).
33 C. Jin, X. Meng, B. Cheng, Z. Li, and D. Zhang, Phys. Rev. B **63**, 195107 (2001).
34 J. K. Yang, C. Schreck, H. Noh, S. F. Liew, M. I. Guy, C. S. O'Hern, and H. Cao, Phys. Rev. A **82**, 053838 (2010).
35 H. Noh, J. K. Yang, S. F. Liew, M. J. Rooks, G. S. Solomon, and H. Cao, Phys. Rev. Lett. **106**, 183901 (2011).
36 M. Xiao, and S. Fan, Phys. Rev. B **96**, 100202 (2017).
37 S. Mansha, and Y. D. Chong, Phys. Rev. B **96**, 121405 (2017).
38 B. Yang, H. Zhang, T. Wu, R. Dong, X. Yan, and X. Zhang, Phys. Rev. B **99**, 045307 (2019).
39 P. Zhou, G. G. Liu, X. Ren, Y. Yang, H. Xue, L. Bi, L. Deng, Y. Chong, and B. Zhang, Light Sci. Appl. **9**, 133 (2020).
40 Z. Xu, X. Kong, R. J. Davis, D. Bisharat, Y. Zhou, X. Yin, and D. F. Sievenpiper, Phys. Rev. Res. **2**, 013209 (2020).
41 J. D. Joannopoulos, S. G. Johnson, J. N. Winn, and R. D. Meade, *Photonic Crystals: Molding the Flow of Light*, 2nd ed. (Princeton University Press, Princeton, 2008).
42 R. Zallen, *The Physics of Amorphous Solids* (Wiley, New York, 1983).
43 P. D. García, R. Sapienza, Á. Blanco, and C. López, Adv. Mater. **19**, 2597 (2007).
44 T. A. Loring, and M. B. Hastings, Europhys. Lett. **92**, 67004 (2010).
45 P. Titum, N. H. Lindner, M. C. Rechtsman, and G. Refael, Phys. Rev. Lett. **114**, 056801 (2015).
46 Y. Ge, and M. Rigol, Phys. Rev. A **96**, 023610 (2017).
47 Z. Qiao, J. Jung, C. Lin, Y. Ren, A. H. MacDonald, and Q. Niu, Phys. Rev. Lett. **112**, 206601 (2014).
48 M. Yan, J. Lu, F. Li, W. Deng, X. Huang, J. Ma, and Z. Liu, Nat. Mater. **17**, 993 (2018).
49 X. Wu, Y. Meng, J. Tian, Y. Huang, H. Xiang, D. Han, and W. Wen, Nat. Commun. **8**, 1304 (2017).
50 L. Zhang, Y. Yang, M. He, H. Wang, Z. Yang, E. Li, F. Gao, B. Zhang, R. Singh, J. Jiang, and H. Chen, Laser Photon. Rev. **13**, 1900159 (2019).